Precision Engineering 95 (2025) 251–261

Contents lists available at ScienceDirect

Precision Engineering

journal homepage: www.elsevier.com/locate/precision

Development of a novel nickel-based metal force microsensor using bottom-up approach

Wojciech J. Dera [a], Hanna Konopacka [b], Dariusz M. Jarząbek [a,b,*]

[a] Institute of Fundamental Technological Research, Polish Academy of Sciences, Warsaw, Poland
[b] Warsaw University of Technology, Warsaw, Poland

ARTICLE INFO

Handling editor: Dr. Masonori Kunieda

Keywords:
Nickel-based sensor
Bottom-up process for sensor fabrication
Electro-galvanic deposition
Capacitance stability
Silicon sensor limitations
Industrial sensor applications
Sensor durability
Displacement-force calibration

ABSTRACT

The advancement of force microsensors has shifted towards alternative fabrication methods offering enhanced flexibility, cost efficiency, and adaptability. Traditional silicon-based sensors face limitations such as mechanical fragility, thermal expansion mismatches, and high fabrication costs, necessitating alternative approaches. This study explores a bottom-up fabrication approach using electro-galvanic deposition to develop nickel-based capacitive force microsensors. Unlike conventional methods, electro-galvanic deposition enables precise control over material thickness and microstructure, allowing for the fabrication of robust, metal-based sensors with superior toughness and mechanical reliability. Nickel, chosen for its high tensile strength, corrosion resistance, and adaptability to high temperatures, is well-suited for demanding applications. The fabrication process involves UV maskless lithography for mold patterning, followed by electro-galvanic deposition in a modified Watt's bath with saccharin additives to control grain structure. This enables fine-tuning of nickel's mechanical properties, enhancing hardness and ductility. The capacitive comb sensor structure, integrated with a high-resolution capacitance-to-digital converter, enables precise force measurements with a linear response and high sensitivity. Experimental validation included mechanical testing, calibration, and stability analysis under controlled loading conditions. Results confirmed a strong linear force-capacitance relationship ($R^2 = 0.9898$) and excellent long-term stability, with minimal capacitance drift under sustained load.

1. Introduction

The development of force microsensors has increasingly turned towards alternative fabrication methods that offer enhanced design flexibility, cost-effectiveness, and adaptability for complex applications [1,2]. While traditional top-down fabrication techniques have been widely used, they often require specialized facilities, high-cost equipment, and impose design constraints due to the inherent limitations of silicon-based processing [3,4]. Silicon microsensors, despite their widespread use, exhibit structural fragility, susceptibility to mechanical damage, and limited fracture toughness, particularly in response to cross-force applications [4]. Additionally, thermal expansion mismatches and residual stresses from conventional microfabrication techniques can further compromise their mechanical reliability [4–7]. Issues such as tribological wear, adhesion-related failures like "stiction," and limitations in achieving non-standard geometries highlight the need for more versatile sensor fabrication approaches [3,8,9]. Furthermore, the cost of silicon processing remains significantly higher than alternative materials, particularly when small-scale production or prototyping is required [3,4].

To address these challenges, this study explores a bottom-up fabrication method based on electro-galvanic deposition [3,10]. Unlike traditional top-down techniques, bottom-up approaches allow for the direct formation of functional structures through controlled material growth, providing greater design freedom without the constraints of subtractive manufacturing [1,10]. Electro-galvanic deposition enables precise control over material deposition, facilitating the fabrication of robust, metal-based force sensors with improved toughness and structural stability [1,2]. Furthermore, this method is highly scalable and does not require the costly infrastructure associated with silicon MEMS processing [1].

In this work, we present the development of a nickel-based capacitive comb sensor utilizing electro-galvanic deposition [10]. The bottom-up nature of this process allows for the creation of highly customizable sensor architectures, leveraging nickel's excellent mechanical robustness and corrosion resistance. This fabrication approach

* Corresponding author. Institute of Fundamental Technological Research, Polish Academy of Sciences, Warsaw, Poland.
E-mail address: djarz@ippt.pan.pl (D.M. Jarząbek).

https://doi.org/10.1016/j.precisioneng.2025.05.003
Received 14 February 2025; Received in revised form 10 April 2025; Accepted 4 May 2025
Available online 5 May 2025

demonstrates significant potential in advancing force-sensing technology by enabling novel sensor designs that are both mechanically durable and adaptable to diverse applications.

2. Experimental

2.1. Material description

Nickel was selected as the sensor material due to its exceptional mechanical and physical properties. Nickel features high mechanical strength, significant wear resistance, and excellent corrosion resistance, making it ideal for applications that require high durability. Its exceptional tensile strength (approximately 380–700 MPa), significantly surpassing that of silicon (165 MPa), combined with its flexibility and capability to withstand high temperatures, makes it well-suited for demanding applications [10,11]. Additionally, nickel demonstrates good electrical and thermal conductivity, which is crucial for constructing sensors that require precise and reliable measurements.

One of nickel's key advantages is its compatibility with electro-galvanic deposition, a bottom-up fabrication technique that enables precise control over the material's thickness and dimensional characteristics. Moreover, by fine-tuning the parameters of the deposition bath and electro-galvanic process, nickel's mechanical properties can be tailored to suit specific application requirements. For example, introducing saccharin into the deposition bath allows for precise control over grain size, ranging from the micrometer to nanometer scale. This, in turn, enables fine-tuning of mechanical properties - nanocrystalline nickel exhibits significantly higher strength but reduced ductility compared to its micrometer-grained counterpart. Such versatility makes nanocrystalline nickel particularly well-suited for applications demanding high stress tolerance.

Hence, the electro-galvanic deposition method used for fabricating nickel microsensors offers extensive customization of sensor characteristics, such as stiffness, yield strength, and resistance to shock loads. By tailoring parameters like bath composition and deposition conditions, the material properties can be optimized for specific application requirements. This adaptability ensures that the nickel sensors are well-suited for a broad range of demanding environments and operational challenges.

2.2. Manufacturing process

The manufacturing process for the nickel microsensors developed in this work is based on electro-galvanic deposition (Fig. 1). It begins with surface preparation (Fig. 1a), a critical step to ensure strong adhesion of the deposited metal. This involves cleaning, activation and polishing of the substrate to create an optimal surface for deposition. Next, a mold for the sensor is created using UV maskless exposure (Fig. 1b). The prepared mold (Fig. 1c) is then immersed in a classical Watt's bath with the addition of saccharin, where nickel is deposited onto the surface through the application of a controlled electric current (Fig. 1d). The process parameters - such as current density, deposition time, and bath temperature - are carefully optimized to achieve uniform and high-quality nickel layers. Experimental conditions, including the pH and nickel ion concentration in the galvanic bath, play a significant role in determining the uniformity and mechanical properties of the deposited nickel. This method, adapted from the work of Jenczyk et al. [10], allows for precise control over layer thickness, which is essential for high-performance sensor fabrication.

2.2.1. Metal substrate

The dimensions of the substrate are 50 mm in diameter and 0.5 mm in thickness. The first step in preparing the metal substrate for the microsensor fabrication process is polishing, which ensures a smooth, uniform surface with roughness below Ra 0.01, necessary for precise metal deposition (Fig. 2a). Polishing is performed using diamond

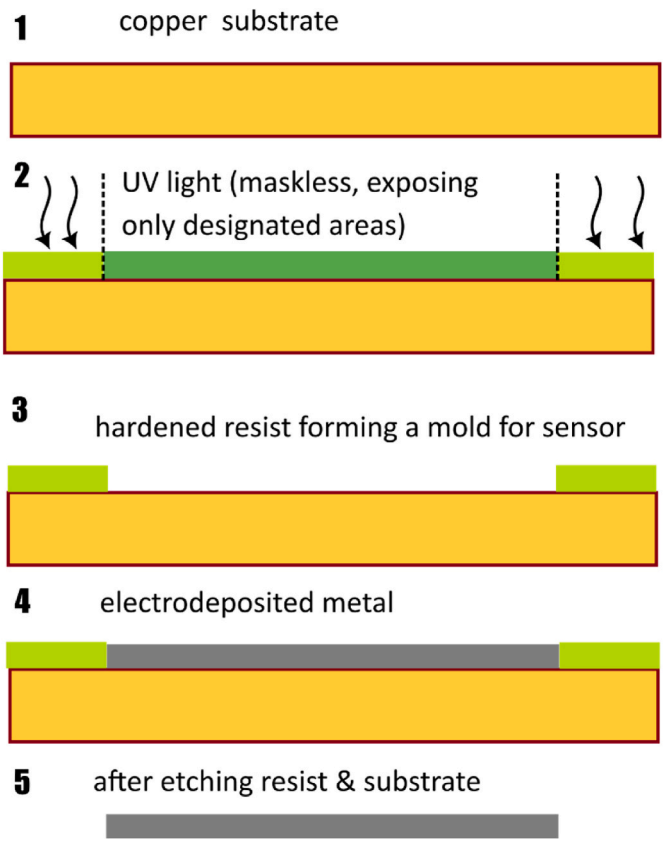

Fig. 1. Process description. a - preparation of the surface of the metal substrate; b - UV maskless exposure; c - mold formation; d - electroplating of metal; e - final microsensor structure.

abrasive slurry with a 1 μm particle size, crucial for eliminating surface imperfections and creating the ideal surface for subsequent layers. Once the polishing is finished, the substrate is ready for cleaning in an ultrasonic bath. Initially, the substrate is immersed in acetone for 5 min to remove organic residues, then it is treated with citric acid to remove any oxide layers that may have formed on the surface, and finally cleaned again in acetone to ensure any remaining citric acid residues are washed away. Then the substrate is rinsed quickly with isopropyl alcohol, ensuring that the surface is free from any contaminants. This step prepares the copper for the application of the TI Prime MicroChemicals GmbH primer. The TI PRIME is applied via spin-coating at 3000 RPM for 20 s. This primer enhances the adhesion of the following layers that will be deposited on the substrate. Following the spin-coating, the substrate is baked at 120 °C for 2 min to secure the primer layer and improve its adhesion properties.

2.2.2. UV maskless exposure and mold formation

The process of applying the MicroChemicals GmbH AZ125nXT photoresist for sensor fabrication involves several steps aimed at achieving precise patterning on the substrate. First, the substrate is prepared by spin-coating the AZ125nXT photoresist at 800 RPM, with a ramp of 0.5 and a dwell time of 20 s. This spin-coating process is repeated three times to achieve a resist layer with a thickness of approximately 300 μm. Once the resist is applied, the substrate undergoes a soft bake, which consists of two temperature stages: the first soft bake at 85 °C for 2 min to remove excess solvent, followed by a second soft bake at 135 °C for 15 min to further solidify the resist. These stages ensure the resist layer is uniformly dried and properly prepared for exposure. Next, the substrate is exposed to UV light with a dose of 14 000 mJ/cm^2 using the Heidelberg μPLA machine. This exposure defines the pattern on the resist layer, which will later be developed. After

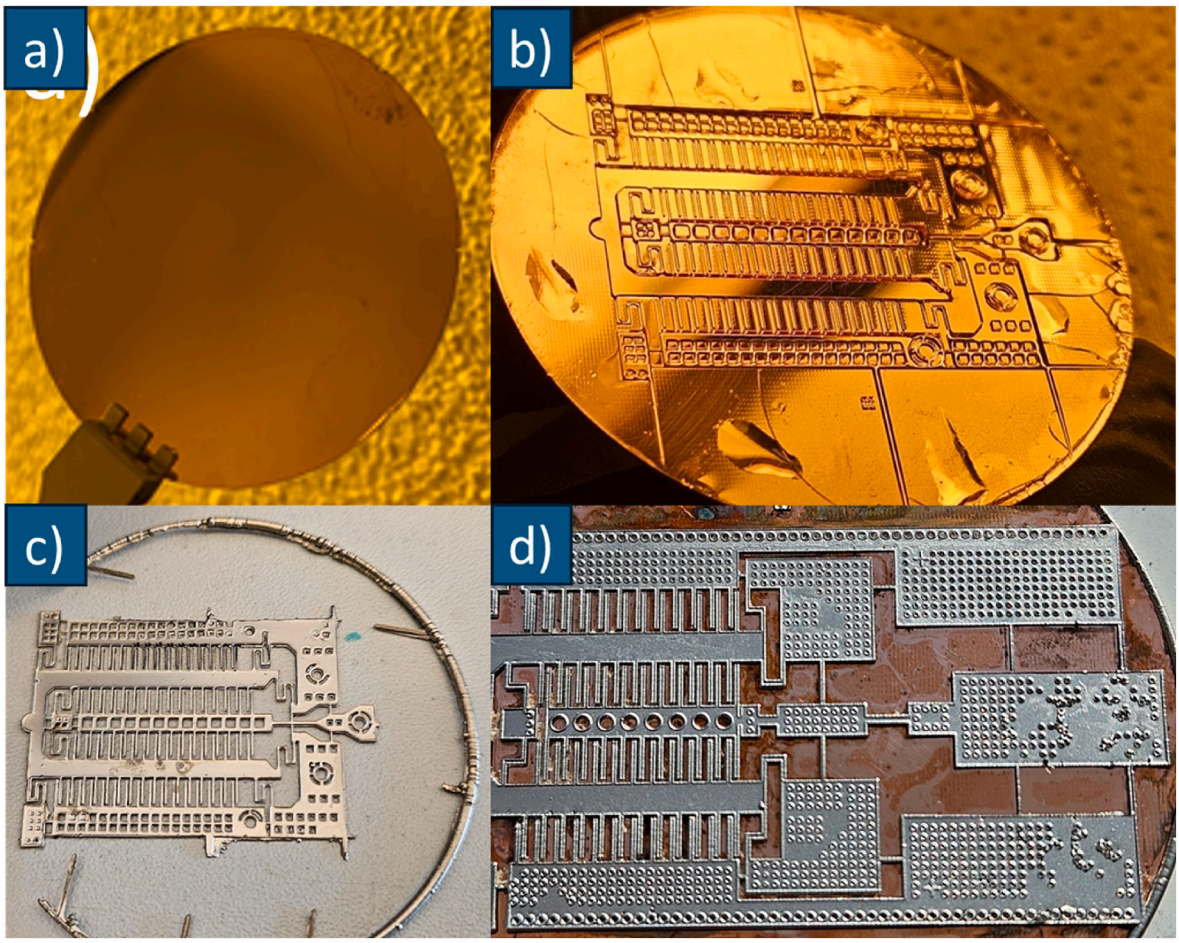

Fig. 2. Images of some initial steps in the sensor fabrication process.
(a) Substrate, (b) Mask prepared and developed, (c) Metal sensor structure cutted from supports, (d) Nickel deposited on copper substrate, mask removed.

exposure, a post-exposure bake (PEB) was performed to ensure the resist pattern became stable and fully crosslinked, as required by the process. Following exposure and any necessary PEB, the substrate is developed using MicroChemicals GmbH AZ 726 MIF developer. This step removes the unexposed resist, leaving behind the desired pattern on the substrate. The final step in the process is hard baking, which ensures that the resist bonds firmly to the substrate. The substrate is placed on a cold hotplate and heated to 135 °C for 15 min. Afterward, the hotplate is turned off, and the substrate is left to cool naturally. The final mold is shown on Fig. 2b. During this cooling phase, it is essential to monitor the resist to ensure that it does not detach from the substrate; if detachment occurs, the process must be restarted.

2.2.3. *Electroplating process*

The electroplating process for the nickel microsensor fabrication involved several key steps, each carefully controlled to ensure optimal metal deposition. The composition of the electroplating bath included nickel salts, additives and other chemicals designed to enhance the plating process. The electroplating bath contained 300 g/l of nickel sulfate ($NiSO_4 \cdot H_2O$), 45 g/l of nickel chloride ($NiCl_2$), 45 g/l of boric acid (H_3BO_3) and a small amount of saccharin (1 g/600 ml) to promote the formation of nanocrystalline nickel. Additionally, sodium lauryl sulfate (SLS) was added at concentrations of 0–0.2 g/l to help control the plating process and potassium chloride (KCl) was included at 10 g/l. All the bath ingredients were purchased from Warchem (Poland). The electroplating process was carried out at a temperature of 60 °C with constant stirring at 200–300 rpm. The plating was performed in two stages. In the first stage, the surface was prepared by removing oxides with an anodic polarization reversal at a current of −0.05 A for 5 s. The second stage involved applying a normal current of 0.15 A for a total of 96 620 s (approximately 26.9 h). This continuous plating process allowed for precise control of the layer thickness, ensuring the formation of a high-quality nickel layer (Fig. 2d).

2.2.4. *Etching of photoresist and substrate*

The final stage of the fabrication process involves etching both the photoresist and the underlying copper substrate to reveal the complete nickel sensor structure. The photoresist, which was used to define the sensor's pattern during the earlier UV exposure step, is removed using a wet etching process. This is accomplished by immersing the substrate in acetone for 30 min, allowing the photoresist to dissolve. The acetone is applied in an ultrasonic bath to ensure effective and thorough removal of the resist layer. Following the removal of the photoresist, the next step is to clean the spaces between the sensor's ribs. This is done by applying acetone under pressure, which effectively removes any residual photoresist or contaminants from the surface. The final step involves selective etching of the copper substrate. A mixture of acetic acid (CH_3COOH), hydrogen peroxide (H_2O_2) and water (H_2O) is used for this purpose. This etching solution selectively removes the copper substrate without affecting the nickel layer, leaving the finished nickel sensor intact. Both acetic acid and hydrogen peroxide were purchased from Warchem (Poland). Once the copper has been etched away, the substrate is thoroughly cleaned to remove any traces of the etching solution, leaving behind the final nickel sensor structure (Fig. 2c). This complete process ensures a clean, well-defined sensor ready for the next steps in testing and integration.

2.2.5. Final mounting on PCB

The sensor was mounted on a dedicated Printed Circuit Board (PCB), securing its position and facilitating the necessary electrical connections. Next, a crucial step in the sensor preparation was the laser-based removal of the supports, ensuring the proper separation of the sensor's three interacting plates (Fig. 3). Close-up views and optical microscope images of the final structure are presented in Fig. 4, illustrating key features such as ribs (Fig. 4a), a stitched full sensor view (Fig. 4b) and springs (Fig. 4c and d).

2.3. Description of characterization method

The sensor underwent a series of mechanical tests, where varying forces were applied to evaluate mechanical strength, sensitivity and signal stability. The sensor's response was continuously recorded, enabling a comprehensive assessment of its performance under different loading conditions. This rigorous testing is vital for understanding both the precision and durability of the sensor, which are essential for reliable operation in real-world applications. The calibration setup allows for the meticulous alignment and measurement necessary for high-precision sensor calibration (Fig. 5a). It consists of a metal plate suspended above a table, attached to supports with flexible cords to isolate it from environmental vibrations. Force measurement was carried out using a calibrated Megatron Elektronik force transducer, model KM1403, with a 100N range and a constant of 2.0357 mV per V. A fused silica spacer (Fig. 5c) is placed at the end of the Calibrated Force Sensor beam, serving as an electrical insulator between the sensor and the metal casing while providing a hard, smooth surface for the sensor tip to glide over. To apply precise displacement, a Thorlabs Z825B linear motor with an incremental encoder and position control was used, ensuring accurate positioning of the sensor.

On the opposite side of the setup, the tested microsensor was mounted with a directly attached AD7746 capacitance converted. Positioning it in close proximity to the sensor minimized interference, enhancing measurement accuracy. A Huvitz HSZ microscope was utilized to monitor the microsensor's behavior during calibration, providing detailed observation of its movement and response to applied forces. Additionally, an X-axis adjustment mechanism with a 0–20 mm range, equipped with an encoder, enabled fine positional adjustments, which were crucial for precise microsensor alignment and calibration accuracy. The working principle of the calibration mechanism, illustrating the interaction between the capacitive force microsensor and the reference system, is depicted in Fig. 5b.

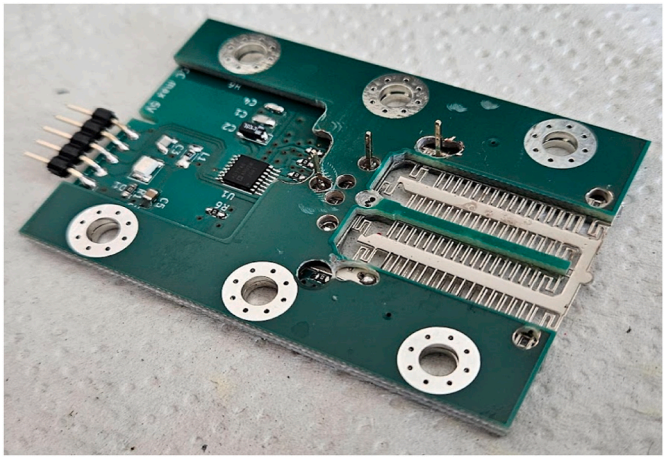

Fig. 3. Prepared sensor on PCB.

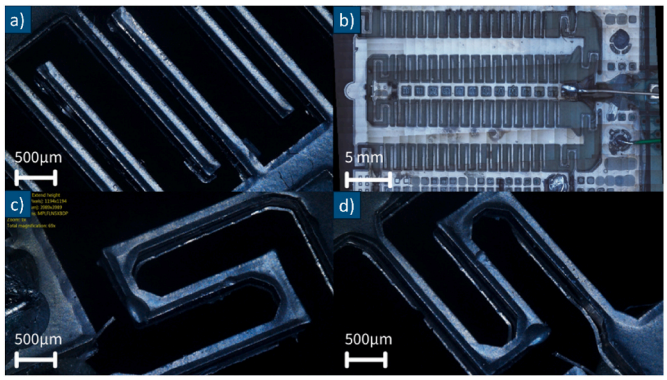

Fig. 4. Optical microscope images of the nickel-based sensor: (a) ribs, (b) stitched full sensor view, (c) first spring, (d) second spring.

2.4. Working principle of differential comb sensor

The mechanical behaviour of the nickel-based capacitive comb microsensor can be described by the relative movement of a moving part with a tip, which displaces under applied force (Fig. 6). The capacitance change between the comb fingers corresponds directly to this displacement. The sensor's design incorporates finger gaps (d_1) and anti-finger gaps (d_2), which influence the overall capacitance response during force application.

As shown in Fig. 6, when a force is applied to the sensor, the movement of the mass in the Y direction causes variations in capacitance between the moving and stationary comb fingers. Specifically, the capacitances C_{1a} and C_{2b} increase, while C_{1b} and C_{2a} decrease. The initial capacitance values are given by:

$$C_{0a} = \frac{\varepsilon A}{d_1}, \quad C_{0b} = \frac{\varepsilon A}{d_2} \qquad \text{Eq. 1}$$

where:

- ε is the permittivity of air,
- A is the effective area between the fingers,
- d_1 is the finger gap spacing,
- d_2 is the anti-finger gap spacing.

When the tip displaces by x under the applied force, the capacitances become:

$$C_{1a} = \frac{\varepsilon A}{d_1 - x}, \quad C_{1b} = \frac{\varepsilon A}{d_2 + x}$$
$$C_{2a} = \frac{\varepsilon A}{d_1 + x}, \quad C_{2b} = \frac{\varepsilon A}{d_2 - x} \qquad \text{Eq. 2}$$

The change in capacitance ΔC is expressed as:

$$\Delta C = (C_{1a} + C_{1b}) - (C_{2a} + C_{2b}) = 2\varepsilon A x \left(\frac{1}{{d_1}^2 - x^2} - \frac{1}{{d_2}^2 - x^2} \right) \qquad \text{Eq. 3}$$

In this design, the anti-finger gap d_2 was chosen based on the geometric constraints of the sensor. If d_2 is comparable to d_1, the resulting ΔC is reduced, impacting sensitivity. When d_2 is significantly larger than d_1, the capacitance change simplifies to:

$$\frac{\Delta C}{x} = 2N_c \varepsilon A \frac{1}{{d_1}^2} \qquad \text{Eq. 4}$$

where N_c is the number of finger pairs. Increasing d_2 allows more flexibility in design but reduces the number of finger pairs, thereby decreasing sensitivity. During sensors design and production, the influence of d_2 on sensitivity must be carefully evaluated. If geometric constraints limit the number of finger pairs, optimizing the anti-finger

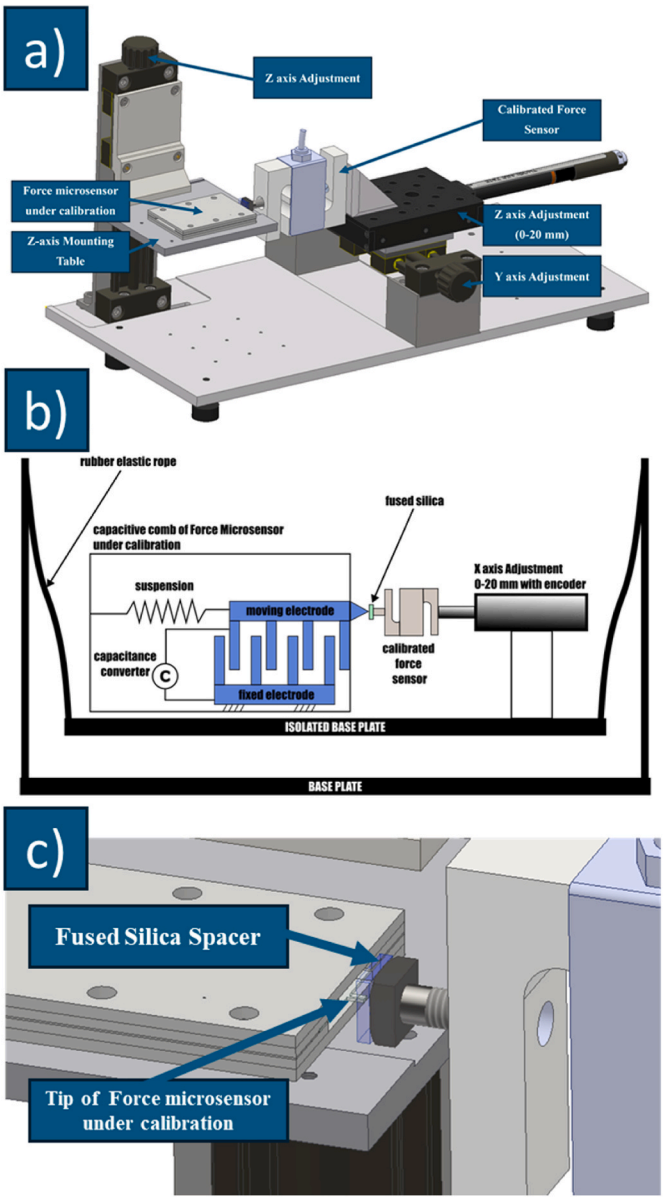

Fig. 5. a) Experimental Setup: the Calibrated Force Sensor, which measures the applied force during calibration; the Z-axis Mounting Table, which secures the Force Microsensor under Calibration; the Z-axis Adjustment for vertical positioning; and the Y-axis Adjustment for lateral positioning, **b) Working Principle:** A schematic diagram illustrating the calibration mechanism of the capacitive force microsensor, **c) Close-up** of the Interface between sensor and Calibrated Force Sensor beam.

gap becomes critical. The detailed process of selecting and calculating the influence of the anti-finger gap on sensor sensitivity is comprehensively described in the publication by Ru Li et al. [12].

2.5. Capacitance converter description

In order to convert the capacitance signal into a digital signal, the high-resolution capacitance-to-digital converter (CDC), based on sigma-delta architecture was used. According to the manufacturer, the converter was designed for direct capacitance measurement. The converter offers two input channels that can be configured as single-ended or differential, providing flexibility for applications with various types of capacitive sensors. The device features exceptional resolution (24 bits with no missing codes, up to 21 bits effective resolution), high linearity (±0.01 %), and excellent accuracy (±4 fF after factory calibration). The input capacitance range is ±4 pF (variable), and the device can also support up to 17 pF of common-mode (fixed) capacitance, which can be compensated using a built-in digitally programmable capacitance converter (CAPDAC). The converter is designed to work with floating (ungrounded) capacitive sensors. The converter also includes an integrated temperature sensor with a resolution of 0.1 °C and an accuracy of ±2 °C, allowing for temperature monitoring during measurements. With an integrated reference voltage and clock generator, the converter requires no additional external components, simplifying its integration into systems. The device also offers a standard voltage input and differential reference input, enabling the connection of an external temperature sensor, such as an RTD, thermistor, or diode, further enhancing its versatility. The formula for converting the sensor reading to capacitance (C_{in}) in picofarads (pF) is presented below:

$$C_{in} = \left(\frac{Code - 0x800000}{0x800000} \times C_{Ref} \right) pF \quad \text{Eq. 5}$$

where:

- *Code* is the value read from the converter,
- C_{Ref} is the reference capacitance value (+4.096 pF).

This formula is applied to process the signal from the AD7746 capacitive sensor, allowing capacitance readings to be expressed in user-friendly units, which is useful for analytical and control purposes. The AD7746 converter is factory-calibrated for a full range of ±4.096 pF. Each unit undergoes individual calibration to ensure high accuracy. The gain factor obtained during factory calibration is stored in one-time programmable (OTP) memory and is copied to the capacitance gain register each time the device is powered on or reset. While operating with the converter, we use a measurement mode with a conversion time of approximately 122 ms. With this setting, the converter achieves a data refresh rate of 8.2 Hz and a bandwidth (−3 dB) of 4.0 Hz. Typical voltage noise values at this setting are as follows:

- RMS noise: 3.0 μV
- Peak-to-peak noise (P-P): 20 μV

In the 122 ms conversion mode, the converter provides an effective resolution of 19.5 bits and a peak-to-peak (P-P) resolution of 16.8 bits. To reduce noise levels, the conversion time for the converter was set to the highest available value - 122.1 ms. Similarly, the conversion time for the built-in temperature converter was also set to 122.1 ms. Therefore, the total conversion time to obtain a complete result (capacitance and temperature) is 231.7 ms, corresponding to a refresh rate of approximately 4.3 Hz. It is worth to note that the converter uses an on-chip transistor to measure the temperature of the silicon core inside the package. The ΔVBE value (base-emitter voltage difference) is converted into a digital signal by the sigma-delta (Σ-Δ ADC) converter. The data is then scaled using factory-set calibration coefficients, making the output code proportional to temperature. The expression for temperature in degrees Celsius is:

$$Temperature\ (^{\circ}C) = \frac{Code}{2048} - 4096 \quad \text{Eq. 6}$$

This allows the converter to provide a direct and accurate reading of the silicon core temperature, enabling monitoring of the operating conditions of the system and correction of capacitance readings in case of temperature changes.

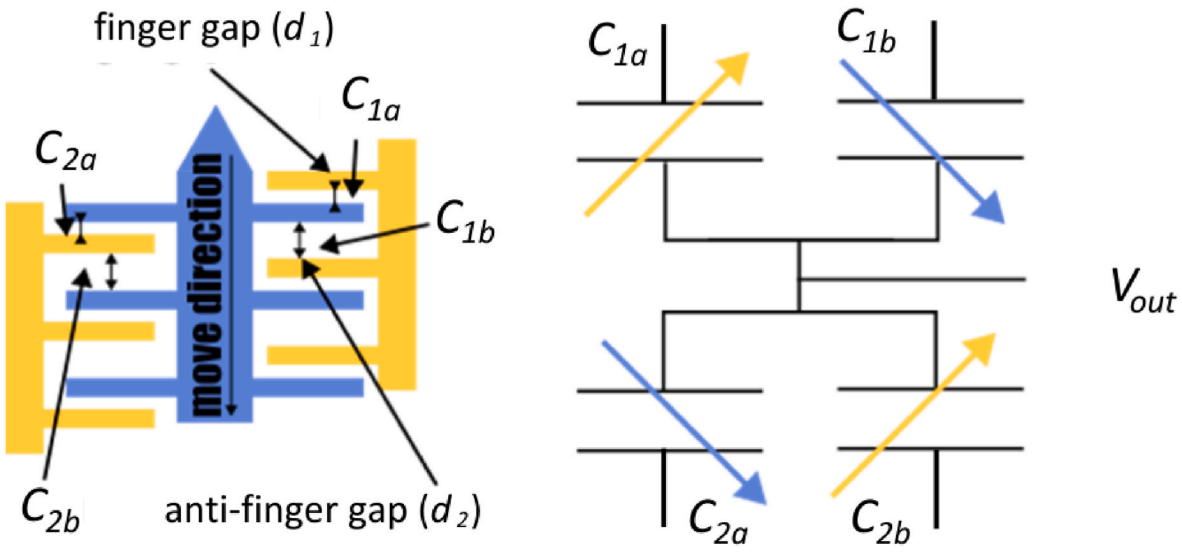

Fig. 6. The comb finger topology and the equivalent circuit.

3. Results

3.1. Analysis of force-capacitance relationship

The relationship between force and capacitance was analysed to determine the sensor constant, which quantifies the sensitivity of the nickel-based microsensor to applied force. A linear motor was used to move the calibrated force sensor into contact with the investigated microsensor at a controlled speed of 0.01 mm/s, while simultaneously recording the force over time and the corresponding capacitance using a capacitance converter (Fig. 7a). During the data processing phase, the capacitance data was aligned with the force data to ensure accurate temporal matching and both datasets were zeroed to remove initial offsets.

To reduce noise and improve clarity, cumulative moving averages were applied to the data, using a 5-sample window to highlight trends (Fig. 7b). To further refine the analysis, the dataset was trimmed to isolate the relevant section of the measurements, ensuring that only the most informative portion of the force-capacitance response was considered (Fig. 7c). The cumulative averages of force versus

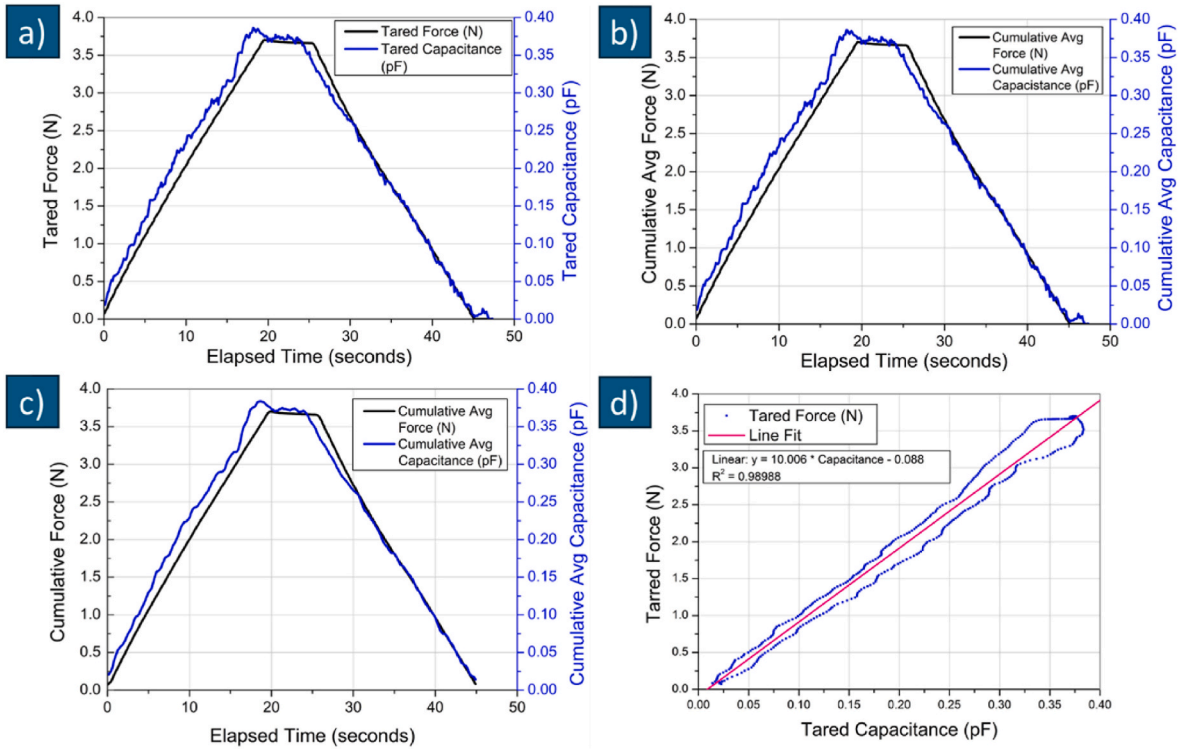

Fig. 7. a) Plot of the tared (zeroed) force and capacitance measurements over elapsed time. Both datasets have been adjusted to start from zero, allowing for a clearer comparison, b) Plot of the cumulative moving average for both force and capacitance measurements, using a 5-sample window. This method smooths the data by averaging every 5 consecutive points, revealing a clearer trend for each measurement, c) Plot of the trimmed cumulative moving average for both force and capacitance, based on the specified start and end times. This view isolates the relevant section of the measurements, allowing for clearer analysis, d) Detailed plot of Force versus Capacitance with a fitted line.

capacitance were then plotted and a linear fit was applied (Fig. 7d). From the slope of this fitted line, the sensor constant was calculated, confirming a consistent linear relationship and validating the sensor's ability to provide precise and reliable measurements.

The plot in Fig. 7d shows the relationship between force and capacitance in finer detail, illustrating how changes in capacitance correspond to applied force values. The fitted line provides a visual representation of the trend, indicating the sensor's sensitivity and response to force. The equation of the fitted line for the detailed Force vs. Capacitance plot is:

$$\begin{aligned} &Force = (10.006 \times Capacitance - 0.088\,N) \pm 0.078\,N \\ &The\ correlation\ coefficient\ (R2) : 0.9898 \end{aligned} \quad \text{Eq. 7}$$

By fitting the force versus capacitance data to a straight line, we determine the sensor's constant for force quantification. The high R^2 value (0.9898) confirms a strong linear correlation, ensuring model accuracy. Minor deviations at higher capacitance values may result from measurement noise or nonlinearity.

3.2. Analysis of force-displacement relationship and spring constant determination

In Fig. 8a the determination of microsensor spring constant is shown. The equation of the fitted line is:

$$\text{Force} = (19.126 \times \text{Displacement} + 0.0994)\ \text{N} \quad \text{Eq. 8}$$

The fitted line provides a slope of 19.126 N/mm, representing the spring constant, and an intercept of 0.0994 N. The standard deviation of the slope is ±0.2001 N/mm, indicating a high level of fit precision. The coefficient of determination R^2 is 0.9986.

In comparison, micro-scale soft springs, such as those used in MEMS devices, typically have spring constants in the range of 0.01–10 N/m. Compression or tension springs in delicate instruments may range from 10 to 1000 N/m, and those in larger mechanical systems usually fall within 1000–5000 N/m. The measured spring constant of 19.126 N/mm is therefore significantly stiffer than typical MEMS springs, aligning with applications requiring higher force resilience. Such stiff microsensors may be used, for example, in micro-compression tests with true displacement control, where the deflection of the microsensor can be considered negligible.

3.3. Capacitance stability test under load

Furthermore, the stability of capacitance over approximately 500 s under a constant applied force of about 2 N was monitored (Fig. 8b). The measurements were conducted using the raw, unprocessed data obtained directly from the microsensor, without calibration or zeroing, to evaluate the microsensor's intrinsic behavior. This approach provided valuable insights into the sensor's performance without the influence of corrections or offsets. The results demonstrated a stable capacitance signal with minor fluctuations around the mean value. The average capacitance was calculated as −0.1030 ± 0.0087 pF, as depicted by the red dashed line in the stability plot (Fig. 8b). Drift is defined as a gradual change in signal over time, as opposed to random fluctuations around a stable mean. A linear trend analysis revealed a capacitance slope −3.39 × 10−5 pF/s with an intercept of −0.0937 pF. Converting the capacitance slope to force using the relationship given on Eq. (7), the drift in force was calculated to be approximately 0.00033 N/s. This minimal positive drift in force suggests a gradual increase over time. While this drift is minor and unlikely to affect most practical applications, it could be significant in highly sensitive measurements. The observed trend highlights the need to monitor and account for such effects in precision systems to ensure accuracy and reliability.

When calibrated and zeroed, the sensor recorded a force of −1.8722 ± 0.0207 N, considering slope uncertainty. By comparison, the reference Calibrated Force Sensor a force of 1.915 N at the end of the same test. These minor discrepancies between the two sensors suggest a small drift or relaxation in the applied load over the measurement period. However, both sensors exhibited consistent behavior, with trends aligning in the same direction. The small differences in recorded forces can be attributed to several factors. One possible explanation is the friction occurring at the interface between the reference sensor and the tested sensor due to small displacements caused by temperature fluctuations and materials flow. Another potential source of discrepancy is the mechanical drift or instability of the test setup, which could influence the readings over time.

Despite these observations, the differences between the sensors are insignificant and do not indicate any fundamental issues with their performance. Instead, the results suggest that the calibration setup itself may require further investigation to mitigate drift or interface-related effects. Future studies should aim to explore these phenomena in more detail, improving the overall accuracy and reliability of the calibration and measurements.

3.4. Verification of the calibrated force sensor

To investigate the potential source of the discrepancies observed during the capacitance stability test, additional experiments were conducted to verify the stability and reliability of the Calibrated Force Sensor. The device was positioned vertically, and weights corresponding to approximately 1 N and 2 N forces were applied. Measurements were recorded over a duration of 500 s for each load condition to assess its response (Fig. 9).

The results confirmed that the system maintained stable readings

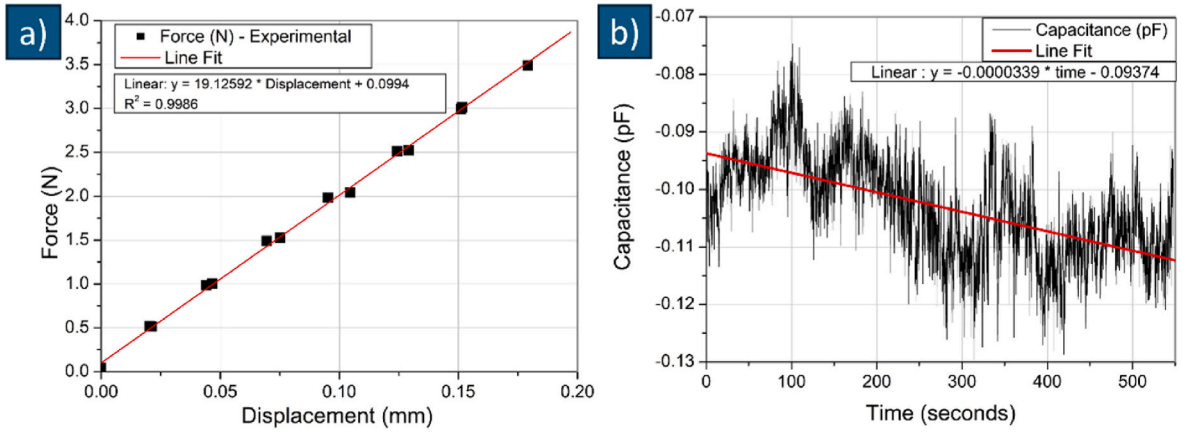

Fig. 8. a) Plot of Force versus Positive Adjusted Displacement with a fitted line, b) Linear Drift Analysis (not tarred).

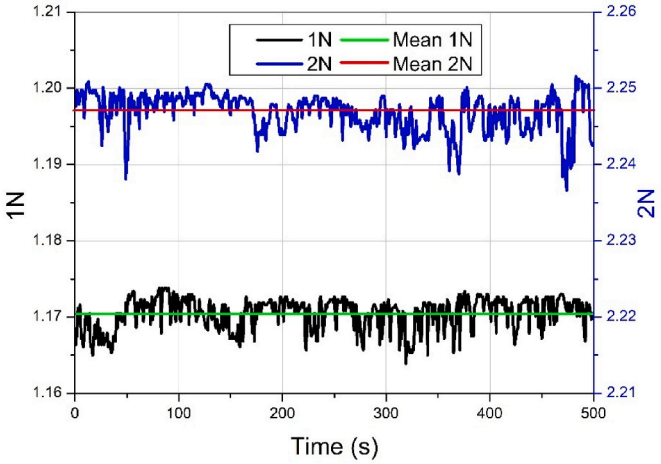

Fig. 9. Stability measurement of the reference sensor under constant load conditions. The left Y-axis represents the 1N data, while the right Y-axis corresponds to the 2N data.

under both load conditions, with no significant drift or relaxation observed. For the 1 N load, the readings remained consistent around the expected value, demonstrating minimal variation. Similarly, under the 2 N load, the sensor exhibited steady behaviour, further validating its reliability as a reference system. These findings ruled out the Calibrated Force Sensor as the source of the observed discrepancies in the capacitance readings.

4. Discussion

The development of nickel-based sensors revealed several challenges, particularly in achieving uniform nickel deposition during the electro-galvanic process. Precise optimization of electrochemical parameters, such as current density and bath temperature, was critical. Minor variations in these parameters often resulted in inconsistencies in the structural properties of the deposited layer, which, in turn, affected sensor performance. Ensuring consistent layer thickness and morphology required meticulous control of the deposition conditions, emphasizing the sensitivity of the electro-galvanic method to external factors.

4.1. Effect of electrochemical parameters on mechanical properties and surface quality

The mechanical and structural quality of the nickel-based sensor is highly sensitive to electrodeposition parameters such as pH, surfactant concentration (e.g., sodium lauryl sulfate – SLS), and the presence of organic additives like saccharin. This sensitivity is well established in the literature. Wasekar et al. demonstrated that saccharin significantly reduces the grain size of nickel coatings, improving hardness due to Hall–Petch strengthening, with observed grain sizes ranging from ~200 nm down to 20 nm depending on the current mode and additive concentration [13].

In our own experiments, we observed a clear correlation between bath pH, SLS concentration, and surface integrity. In particular, when the pH was not maintained close to 4 and the SLS concentration was suboptimal, surface defects such as gas bubbles and delamination appeared. The presence of such defects compromised mechanical integrity and rendered sensors unusable (Fig. 10a).

As shown in the 3D surface inspection (Fig. 10b), gas bubbles formed during deposition locally adhered to the nickel surface, preventing uniform metal growth. In some cases, these bubbles attached directly to the structural ribs (Fig. 10c), leading to localized thinning and, ultimately, mechanical failure of the rib due to stress concentration.

Furthermore, the influence of saccharin on microstructure and hardness observed in our process is consistent with prior reports. As reported by El-Sherik et al. [14] and Wasekar et al. [13], saccharin acts as a grain refiner and adsorptive growth inhibitor, leading to enhanced hardness in the range of 200–500 HV depending on concentration and deposition regime. In our deposition setup, hardness values increased from ~240 HV (without additive) to ~480 HV (with saccharin), confirming the effect. These findings underscore the need for precise control of deposition chemistry to achieve reproducible and high-performance sensor elements.

4.2. Structural anomalies during high-force loading

Another significant challenge was calibration for accurate force measurements. Capacitance peaks observed between 3 and 5 N during force application (Fig. 11) suggested deviations of the sensor from its intended measurement plane. These anomalies likely resulted from mechanical misalignments or slack within the setup, necessitating a

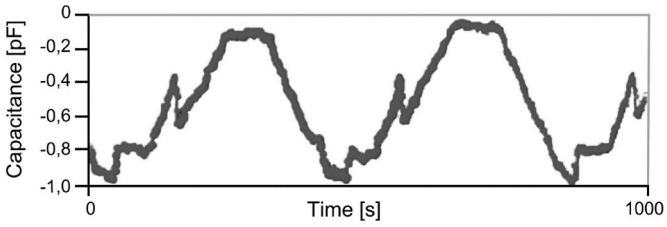

Fig. 11. Capacitance response of the nickel-based sensor during force application, showing an unexpected peak between 3 and 5 N. This anomaly indicates potential deviations from the intended measurement plane, highlighting challenges in sensor calibration.

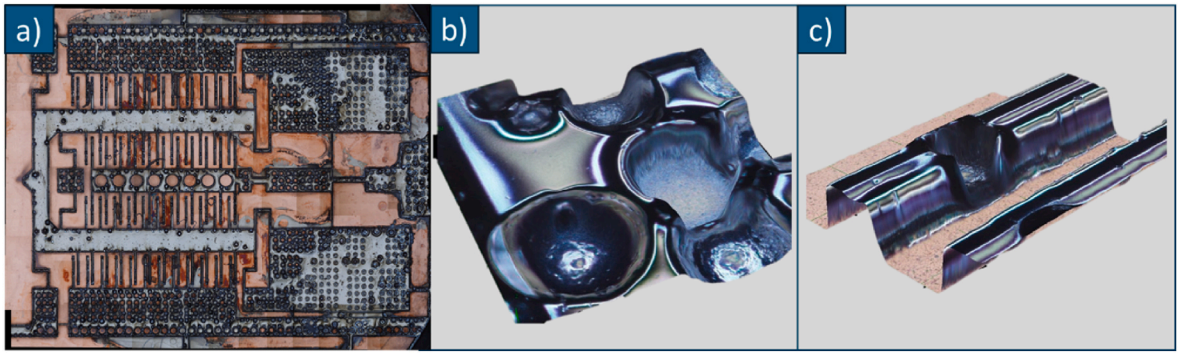

Fig. 10. Surface degradation due to improper electrodeposition: a) optical image of the sensor showing deposition irregularities, b) gas bubble imprint on nickel layer, c) bubble-induced thinning of structural rib.

limitation of the sensor's effective operating range. This issue underscored the importance of precise mechanical alignment during both sensor fabrication and experimental testing.

High-magnification optical inspection of the sensor structure under increasing loads revealed a localized out-of-plane deflection of the central rib above approximately 3 N, consistent with elastic buckling, as illustrated in Fig. 12.

This deformation is consistent with elastic buckling, a phenomenon where a structural element deviates laterally from its load axis due to compressive instability. Since the sensor is designed as a planar structure with a long, thin rib spanning the active region, it is particularly susceptible to Euler-type buckling under axial compressive loads.

The capacitance peak observed between 3 and 5 N thus likely results from a transient decrease in effective electrode overlap area as the rib deflects away from the opposing plate. This geometrical change temporarily alters the capacitance signal until the structure either stabilizes or the deformation becomes irreversible. This hypothesis is supported by the reversibility of the signal at lower loads and the absence of permanent plastic deformation post-test.

These observations underscore the importance of maintaining rib geometry within critical slenderness limits to avoid mechanical instability during high-force operation. Additional FEM simulations or high-speed displacement tracking may help further quantify the onset of this elastic instability in future work.

4.3. Calibration challenges and strategies for improvement

To address these calibration challenges and improve measurement accuracy, it is recommended to integrate a capacitive displacement sensor onto the load-bearing component of the system. This enhancement would enable direct measurement of displacement, independent of any mechanical play or slack, particularly at reversal points where backlash effects are most pronounced. By capturing true displacement values, this approach would eliminate inaccuracies caused by mechanical misalignments, significantly enhancing the reliability of the displacement-force relationship. In summary, while the development of nickel-based sensors showcased the potential of the electro-galvanic method, it also highlighted the need for precise control during both fabrication and experimental setup. Implementing displacement measurement enhancements would ensure higher data fidelity and provide a robust foundation for further research and application development.

4.4. Scalability and fabrication flexibility of the bottom-up method

Finally, this study demonstrates the potential of nickel-based microsensors fabricated through electro-galvanic deposition. A key strength of this approach lies in its flexibility and adaptability, enabling the production of sensors tailored to specific applications without the need for costly and rigid manufacturing infrastructure. Unlike conventional top-down methods used for silicon-based sensors, this bottom-up technique allows for precise control over the material's structural properties, such as layer thickness and morphology. This flexibility provides opportunities to create sensors with a wide range of force sensitivities, geometries, and functional characteristics to meet diverse operational requirements. The electro-galvanic deposition process also emphasizes simplicity and scalability. In a laboratory setting, it is possible to produce small batches of customized sensors using readily available and cost-effective equipment. This contrasts with the production of silicon-based MEMS sensors, which typically require expensive facilities and significant initial investment. The ability to quickly adapt the fabrication process to new designs or application needs highlights the scalability and practicality of nickel-based sensors.

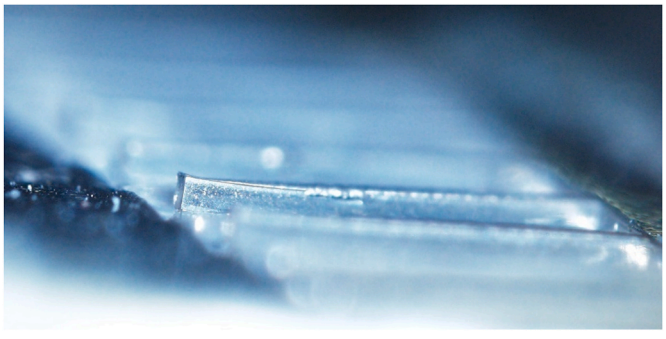

Fig. 12. Out-of-plane deflection of many of the central ribs above 3 N, captured under optical microscope.

Although a 50 mm copper disc was used as the substrate in this study, this size was selected solely for convenience and availability. The electro-galvanic deposition process itself imposes no restrictions on substrate dimensions or shape. It can be performed on flat metallic sheets of arbitrary size, including large panels or foils commonly used in printed circuit board (PCB) fabrication. Multiple sensors can be deposited simultaneously on a single substrate and later separated by laser cutting or mechanical processing.

This capability enables straightforward scaling of the process toward batch fabrication, offering a flexible and cost-efficient alternative to silicon wafer-based MEMS manufacturing. The bottom-up approach is thus compatible with both low-volume prototyping and high-throughput production of force sensors in diverse formats.

Additionally, two critical aspects distinguishing the proposed sensor from MEMS devices are its extended mechanical range and the strategy adopted for parasitic capacitance suppression.

Compared to commercially available MEMS-based capacitive force sensors, which are typically optimized for sub-newton force measurements with resolutions in the nanonewton to micronewton range (e.g., ±2 N range and 5 μN resolution), the nickel-based sensor presented in this study operates in a different regime. While the particular prototype evaluated here exhibited geometric instability above 3 N due to rib deflection, the underlying fabrication method allows for design scaling and structural reinforcement to support significantly higher loads.

This makes the sensor more suited for applications requiring mechanical durability, structural load sensing, or in-house calibration rather than high-resolution force measurements. Its fabrication simplicity and tolerance to high forces make it a viable option for custom setups and research instrumentation where traditional MEMS sensors may be too fragile or cost-prohibitive.

Regarding signal integrity, special attention was devoted to minimizing parasitic capacitance effects. The differential readout system (AD7746) was placed in close proximity to the active sensing area to limit stray capacitance introduced by long wires or PCB traces. The sensor layout ensures that only the intended electrodes contribute significantly to the measured capacitance, and surrounding structures were electrically shielded or grounded where applicable. Further suppression of environmental coupling is achieved by using differential measurement mode and configuring CAPDAC compensation registers. These design strategies significantly improve measurement fidelity and reduce susceptibility to noise and drift.

In terms of sensitivity, the current prototype demonstrates a capacitive response of approximately 0.1 pF/N, based on linear regression of the measured capacitance-force relationship in the range of 0–3.5 N (Fig. 7). While this is lower than the sensitivity of some commercial silicon-based capacitive force sensors — which can exceed 2 pF/N in the ±2 N range — it is nonetheless sufficient for high-force measurements where robustness and structural integrity are prioritized. The lower sensitivity in our design results from larger electrode spacing and structural geometry optimized for mechanical strength rather than resolution.

Temperature effects were not systematically evaluated in this study. However, the sensor employs a fully differential electrode configuration, where active and reference electrodes are symmetrically connected to

suppress drift caused by thermal expansion or dielectric fluctuations. This approach is commonly used in high-precision commercial sensors. Furthermore, the AD7746 readout circuit includes an integrated temperature sensor, which enables thermal compensation in future revisions of the system.

While silicon-based capacitive sensors often exhibit thermal drift in the range of 100–1000 ppm/°C due to material properties and residual stress [15], electroplated nickel structures are expected to demonstrate more stable and predictable thermal behavior. This assumption is supported by recent studies on nanocrystalline nickel coatings, which show that appropriately controlled grain size enhances both thermal stability and resistance to microstructural degradation under thermal load [16]. Future work will include thermal cycling experiments to quantify and, if needed, compensate temperature-induced effects in the developed sensor.

4.5. Comparative summary

To further contextualize the performance and applicability of the proposed nickel-based sensor, Table 1 summarizes key differences in fabrication methods and operational parameters compared to conventional silicon-based MEMS sensors. While the prototype was designed for robustness rather than sensitivity, it demonstrates sufficient performance for high-force measurement applications. Its fabrication method allows for flexible geometry, substrate independence, and cost-efficient batch production. These features make the device particularly attractive for research tools, calibration instruments, and conditions where conventional MEMS sensors may be too fragile or expensive.

Electroplated nanocrystalline nickel also offers inherent thermal stability under moderate operating conditions, which may be beneficial in environments with fluctuating temperature. A comparison of representative parameters is provided below.

Table 1
Comparison of fabrication methods and performance metrics for the proposed nickel-based sensor and typical silicon MEMS sensors.

Parameter	Proposed Nickel Sensor	Typical Silicon MEMS Sensor
Fabrication method	Bottom-up electrodeposition	Top-down photolithography & etching
Substrate size limitation	None (scalable)	Wafer-based (commonly ≤ 6")
Sensitivity (pF/N)	~0.1	0.5–2.0
Max force without failure	>3 N	<1 N typical
Temperature coefficient	Estimated low; differential layout & metal stability	100–1000 ppm/°C
Fabrication cost	Low, lab-scale	High (requires cleanroom)
Batch fabrication possibility	Yes	Yes
Geometrical customization	High	Limited

4.6. Outlook and future work

While the sensors developed in this study are physically larger than typical MEMS-based devices, their robust design and bottom-up fabrication process provide distinct advantages in mechanical durability and structural integrity. The increased size is primarily dictated by experimental constraints and the use of planar substrates during prototyping. However, the fabrication approach remains fully scalable and adaptable, enabling future miniaturization if required.

Future research will focus on several key directions. First, the integration of external or embedded displacement sensors will allow for direct measurement of deformation and enable more accurate force reconstruction, particularly in applications sensitive to hysteresis or mechanical slack. Second, thermal characterization and compensation strategies, including temperature cycling, real-time correction, and grain-structure optimization will be explored to enhance sensor stability under varying environmental conditions. Finally, finite element modeling (FEM) will be employed to refine rib geometry and predict buckling thresholds, paving the way for sensors optimized for specific force ranges and loading profiles.

5. Conclusions

This study confirms the feasibility of using electroplated nickel to fabricate capacitive force sensors via a bottom-up method. The approach enables robust, customizable, and low-cost sensor structures suited for high-force applications.

The prototype showed good sensitivity, linearity, and repeatability, despite challenges in deposition control and calibration. The method offers design freedom beyond silicon-based MEMS processes, allowing adaptation to specific needs.

Future improvements should focus on temperature compensation, displacement measurement integration, and miniaturization. With these enhancements, nickel-based sensors may become a strong alternative to conventional MEMS devices in demanding conditions.

CRediT authorship contribution statement

Wojciech J. Dera: Writing – original draft, Visualization, Methodology, Investigation, Funding acquisition, Formal analysis, Data curation. **Hanna Konopacka:** Writing – review & editing, Visualization, Methodology, Investigation. **Dariusz M. Jarząbek:** Writing – review & editing, Validation, Supervision, Resources, Methodology, Conceptualization.

Declaration of generative AI and AI-assisted technologies in the writing process

During the preparation of this work the author(s) used ChatGPT by OpenAI in order to correct the spelling and English grammar. After using this tool, the authors reviewed and edited the content as needed and take full responsibility for the content of the publication.

Declaration of competing interest

The authors declare that they have no known competing financial interests or personal relationships that could have appeared to influence the work reported in this paper.

Acknowledgments

The authors would like to acknowledge the support of the National Center for Research and Development in Poland through grant TANGO-IV-B/0002/2019 and National Science Centre through grant 2021/41/N/ST5/02920 for partially supporting the research.

References

[1] Lim CS, Niwa T, Watanabe S, Zhang C, Guan A, Mitsuoka Y, et al. Fabrication of void-free submillimeter-scale nickel component by bottom-up electrodeposition. J Phys Commun 2021;5:025001. https://doi.org/10.1088/2399-6528/abdc4f.
[2] Raub E. Galvanische legierungsniederschläge. Chem Ing Tech 1973;45:167–74. https://doi.org/10.1002/cite.330450407.
[3] Ayón AA, Braff R, Lin CC, Sawin HH, Schmidt MA. Characterization of a time multiplexed inductively coupled plasma etcher. J Electrochem Soc 1999;146:339–49. https://doi.org/10.1149/1.1391611.
[4] Spearing SM. Materials issues in microelectromechanical systems (MEMS). Acta Mater 2000;48:179–96. https://doi.org/10.1016/S1359-6454(99)00294-3.
[5] Evans AG, Hutchinson JW. The thermomechanical integrity of thin films and multilayers. Acta Metall Mater 1995;43:2507–30. https://doi.org/10.1016/0956-7151(94)00444-M.

[6] Smith DL, Hoffman DW. Thin-film deposition: principles and practice. Phys Today 1996;49:60–2. https://doi.org/10.1063/1.2807590.
[7] Ohring Milton. Materials science of thin films: deposition and structure. second ed. Academic Press; 2002.
[8] Bhushan B. Tribology issues and opportunities in MEMS. Proceedings of the NSF/AFOSR/ASME workshop on tribology issues and opportunities in MEMS held in Columbus. 1997. p. 9–11. Ohio, USA.
[9] Sniegowski JJ, Garcia EJ. Surface-micromachined gear trains driven by an on-chip electrostatic microengine. IEEE Electron Device Lett 1996;17:366–8. https://doi.org/10.1109/55.506369.
[10] Jenczyk P, Gawrońska M, Dera W, Chrzanowska-Giżyńska J, Denis P, Jarząbek DM. Application of SiC particles coated with a protective Ni layer for production of Ni/SiC co-electrodeposited composite coatings with enhanced tribological properties. Ceram Int 2019;45:23540–7. https://doi.org/10.1016/j.ceramint.2019.08.063.
[11] Greiner F, Schlaak HF. High aspect ratio metal micro and nano pillars for minimal footprint MEMS suspension. Microsyst Technol 2013;19:425–31. https://doi.org/10.1007/s00542-012-1659-x.
[12] Li R, Mohammed Z, Rasras M, Elfadel I, Abe M, Choi D. Design, modelling and characterization of comb drive MEMS gap-changeable differential capacitive accelerometer. Measurement 2021;169:108377. https://doi.org/10.1016/j.measurement.2020.108377.
[13] Wasekar NP, Haridoss P, Seshadri SK, Sundararajan G. Influence of mode of electrodeposition, current density and saccharin on the microstructure and hardness of electrodeposited nanocrystalline nickel coatings. Surf Coat Technol 2016;291:130–40. https://doi.org/10.1016/j.surfcoat.2016.02.024.
[14] El-Sherik AM, Erb U, Page J. Microstructural evolution in pulse plated nickel electrodeposits. Surf Coat Technol 1997;88:70–8. https://doi.org/10.1016/S0257-8972(96)02928-3.
[15] Li H, Zhai Y, Tao Z, Gui Y, Tan X. Thermal drift investigation of an SOI-based MEMS capacitive sensor with an asymmetric structure. Sensors 2019;19:3522. https://doi.org/10.3390/s19163522.
[16] Julie S, Wasekar NP, Parida PK, Santra S, David C, Kamruddin M. Effect of grain size on the thermal stability of electrodeposited nanocrystalline nickel: X-ray diffraction studies. Thin Solid Films 2022;745:139114. https://doi.org/10.1016/j.tsf.2022.139114.